Journal of the American College of Cardiology
© 2012 by the American College of Cardiology Foundation
Published by Elsevier Inc.

Vol. 60, No. 7, 2012
ISSN 0735-1097/$36.00
http://dx.doi.org/10.1016/j.jacc.2012.02.053

PRE-CLINICAL RESEARCH

Cardiovascular and Systemic Microvascular Effects of Anti-Vascular Endothelial Growth Factor Therapy for Cancer

J. Todd Belcik, BS, RDCS,* Yue Qi, MD,* Beat A. Kaufmann, MD,* Aris Xie, BS,* Sherry Bullens, BA,† Terry K. Morgan, MD, PHD,‡ Susan P. Bagby, MD,§ Ganesh Kolumam, PHD,† Joe Kowalski, BS,† Jon A. Oyer, PHD,‖ Stuart Bunting, PHD,† Jonathan R. Lindner, MD*

Portland, Oregon; and South San Francisco, California

Objectives This study sought to evaluate the contribution of microvascular functional rarefaction and changes in vascular mechanical properties to the development of hypertension and secondary ventricular remodeling that occurs with anti-vascular endothelial growth factor (VEGF) therapy.

Background Hypertension is a common side effect of VEGF inhibitors used in cancer medicine.

Methods Mice were treated for 5 weeks with an anti-murine VEGF-A monoclonal antibody, antibody plus ramipril, or sham treatment. Microvascular blood flow (MBF) and blood volume (MBV) were quantified by contrast-enhanced ultrasound in skeletal muscle, left ventricle (LV), and kidney. Echocardiography and invasive hemodynamics were used to assess ventricular function, dimensions and vascular mechanical properties.

Results Ambulatory blood pressure increased gradually over the first 3 weeks of anti-VEGF therapy. Compared with controls, anti-VEGF–treated mice had similar aortic elastic modulus and histological appearance, but a marked increase in arterial elastance, indicating increased afterload, and elevated plasma angiotensin II. Increased afterload in treated mice led to concentric LV remodeling and reduced stroke volume without impaired LV contractility determined by LV peak change in pressure over time (dp/dt) and the end-systolic dimension–pressure relation. Anti-VEGF therapy did not alter MBF or MBV in skeletal muscle, myocardium, or kidney; but did produce cortical mesangial glomerulosclerosis. Ramipril therapy almost entirely prevented the adverse hemodynamic effects, increased afterload, and LV remodeling in anti-VEGF–treated mice.

Conclusions Neither reduced functional microvascular density nor major alterations in arterial mechanical properties are primary causes of hypertension during anti-VEGF therapy. Inhibition of VEGF leads to an afterload mismatch state, increased angiotensin II, and LV remodeling, which are all ameliorated by angiotensin-converting enzyme inhibition.
(J Am Coll Cardiol 2012;60:618–25) © 2012 by the American College of Cardiology Foundation

Antagonists to vascular endothelial growth factor (VEGF) such as humanized anti-human monoclonal antibodies (mAbs) and small molecule inhibitors of VEGF signaling are commonly used to treat cancers (1). These drugs are associated with a high incidence of hypertension and proteinuria (2–5). Several potential mechanisms for hypertension have been proposed. Systemic capillary rarefaction could contribute to hypertension by increasing vascular resistance, although there is still ambiguity regarding whether capillary regression during VEGF inhibition is widespread throughout the systemic circulation, or confined to specific vulnerable beds such as the thyroid, the trachea, the intestinal villi, and the skin (2,6–9). Hypertension from VEGF inhibitors could also be secondary to increased vascular tone that occurs from a reduction in VEGF receptor–mediated nitric oxide (NO) produc-

See page 626

From the *Division of Cardiovascular Medicine, Oregon Health & Science University, Portland, Oregon; †Department of Tumor Biology and Angiogenesis, Genentech Inc., South San Francisco, California; ‡Department of Pathology, Oregon Health & Science University, Portland, Oregon; §Division of Nephrology and Hypertension, Oregon Health & Science University, Portland, Oregon; and the ‖Vollum Institute, Oregon Health & Science University, Portland, Oregon. This study was supported in part by a grant from Genentech Inc. Dr. Kaufmann is supported by a research grant from the Lichtenstein Foundation. Dr. Morgan is supported by the Office of Research on Women's Health and the National Institute of Child Health and Human Development, Oregon BIRCWH HD043488-08. Dr. Lindner is supported by grants R01-HL-078610, R01-DK-063508, and RC1-HL-100659 from the National Institutes of Health. All other authors have reported that they have no relationships relevant to the contents of this paper to disclose.

Manuscript received November 3, 2011; revised manuscript received February 2, 2012, accepted February 6, 2012.

tion (10,11), or from a rise in circulating vasoconstrictors such as endothelin-1 or angiotensin II (12). Renal effects of VEGF inhibition such as thrombotic microangiopathy or renovascular dysregulation may also contribute to hypertension (4,6,13,14). The relative contribution of these events to hypertension is uncertain.

In this study, we characterized the cardiovascular adaptations and multiorgan in vivo microvascular changes associated with hypertension during anti-VEGF therapy in mice. The microcirculation in the heart, kidney, and skeletal muscle was assessed with contrast-enhanced ultrasound (CEU), which provides quantitative information on not only microvascular blood flow (MBF), but also microvascular blood volume (MBV). This technique is able to evaluate *functional* microvascular density, which is not necessarily equivalent to *anatomic* microvascular density, in many tissues such as the heart and skeletal muscle, where only a fraction of capillaries are functionally patent at rest (15,16). Comprehensive evaluation of cardiac function and vascular mechanical properties were performed using echocardiography and invasive manometry; whereas histology was used to evaluate pathological changes in the kidney and the aorta.

Abbreviations and Acronyms

CEU = contrast-enhanced ultrasound
LV = left ventricle/ventricular
mAb = monoclonal antibody
MBF = microvascular blood flow
MBV = microvascular blood velocity
MHC = myosin heavy chain
PAS = periodic acid–Schiff
rt-PCR = real-time polymerase chain reaction
SBP = systolic blood pressure
SV = stroke volume
VcF = velocity of circumferential shortening
VEGF = vascular endothelial growth factor

Methods

Study design. The study protocol was approved by the Institutional Animal Care and Use Committee at Oregon Health & Science University. Wild-type C57Bl/6 mice (n = 83) and double-knockout mice (n = 50) produced by gene-targeted deletion of the low-density lipoprotein receptor and Apobec-1 mRNA editing peptide for apolipoprotein B were studied. The latter group was used to study whether effects of VEGF inhibition were amplified in a model of pre-atherosclerotic hyperlipidemia. Baseline studies were performed at 10 to 12 weeks of age and were repeated after 5 weeks of either: 1) treatment biweekly with a phage-derived anti-murine VEGF-A mAb (G6-31, Genentech, South San Francisco, California) (10 mg/kg intraperitoneally; 2) treatment with G6-31 and the angiotensin-converting enzyme inhibitor ramipril (5 mg/kg/day) added to the drinking water; or 3) control injection with vehicle or ragweed pollen. For imaging protocols, mice were anesthetized with 1.0% to 1.5% inhaled isoflurane.

Echocardiography. Echocardiography (Vevo-770, VisualSonics, Toronto, Ontario, Canada) was performed using a high-frequency (40 MHz) transducer. See the Online Appendix for methods for evaluating left ventricular (LV) dimensions, systolic function, and stroke volume (SV).

Hemodynamic measurements. Invasive hemodynamic measurements were performed only after completion of therapy. A calibrated 1.4-F catheter-tip micromanometer (SPR-671, Millar Instruments, Houston, Texas) was inserted into the carotid artery and advanced retrograde into the aorta. Systolic (SBP) and diastolic blood pressures were recorded, after which the catheter was advanced briefly into the LV to measure peak positive and negative dp/dt. Aortic pulse pressure (Δp) was combined with aortic diameter measurements (D) to calculate aortic elastic modulus by: $(\Delta p \times D_d)/\Delta D$, where D_d is aortic diastolic diameter. Arterial elastance was calculated by: $(0.9 \times SBP)/SV$ (17).

Ambulatory blood pressure. Conscious ambulatory blood pressure was measured using a carotid artery catheter interfaced with a radiotelemetry pressure transducer (PA-C10, Data Sciences International, St. Paul, Minnesota). After allowing several days for recovery, pressure measurements were recorded at baseline and twice weekly for 5 weeks after starting therapy with G6-31 (n = 10) or control (ragweed pollen) injections (n = 9).

Microvascular perfusion and blood volume. Lipid-shelled decafluorobutane microbubbles were prepared (18). Perfusion imaging of the myocardium, proximal hindlimb adductor skeletal muscle, and kidney was performed using a linear-array transducer (Sequoia 512, Siemens Medical Systems, Malvern, Pennsylvania). The nonlinear fundamental (7 MHz) signal component from the contrast agent was detected using multipulse phase inversion and amplitude modulation at a mechanical index of 0.2. Blood pool signal (I_{LV}) was measured from a region of interest placed in the LV cavity at end-diastole during a microbubble infusion rate of 5×10^5 min^{-1}. Microbubble infusion rates were increased to 5×10^6 min^{-1} for myocardial and renal perfusion imaging, and 1×10^7 min^{-1} for skeletal muscle perfusion. Time-intensity data were acquired after a high-power (mechanical index: 1.1) 5-frame sequence and were fit to the function: $y = A(1 - e^{\beta t})$, where y is intensity at time t, A is the plateau intensity, and the rate constant $-\beta$ is the microvascular flux rate (15,19). MBV was quantified by $(A)/(1.06 \times I_{LV} \times F \times 0.9)$, where 1.06 is tissue density (g/cm^3), F is the scaling factor for the different infusion rate for I_{LV}, which was reduced to avoid dynamic range saturation, and 0.9 is a coefficient to correct for murine sternal attenuation determined a priori. MBF was quantified by the product of MBV and β. In skeletal muscle, MBV in the capillary compartment alone was measured by eliminating signal from vessels with a velocity of >2 mm/s (15). Skeletal muscle MBF during exercise was measured after 2 min of electrostimulated (5 mA) contraction of the adductor muscles at 2 Hz. Renal vascular resistance was calculated by the mean arterial pressure divided by the renal MBF.

PCR for markers of hypertrophy and remodeling β-myosin heavy chain mRNA. The mRNA for β-myosin heavy chain (MHC), atrial natriuretic peptide (ANP), and B-type natriuretic peptide (BNP) was measured by real-time polymerase chain reaction (rt-PCR) (Online Appendix).

Endothelial nitric oxide synthase phosphorylation. Phosphorylation of endothelial nitric oxide synthase (eNOS), which occurs downstream from VEGF receptor activation, was evaluated by enzyme-linked immunosorbent assay from cardiac muscle samples (Online Appendix).

Histology. For renal histology, periodic acid–Schiff (PAS) staining of fixed paraffin-embedded coronal sections was performed. Sections were evaluated in triplicate blinded to treatment. Glomerular and tubulointerstitial injury were scored as 0 = absent, 1 = mild focal, 2 = moderate multifocal, or 3 = severe diffuse cortical involvement. Renal immunohistology was performed using hamster anti-mouse CD31 (MAB1398Z, Chemicon/Millipore, Billerica, Massachusetts) primary and Cy3-labeled secondary mAbs. Fibrin staining was performed with fluorescein isothiocyanate–labeled anti-fibrinogen/fibrin primary mAb (AXL234F, Accurate Chemical, Westbury, New York). Skeletal muscle microvascular density was assessed by immunohistochemistry with a Cy3-labeled smooth muscle α-actin mAb (1A4, Sigma, St. Louis, Missouri) and was expressed by the total microvessel area per muscle section area. Myocardial collagen content was quantified by the percent area positive for picrosirius red staining under polarized light. Myocyte cross-sectional area was measured from 15 to 25 myocytes from >5 separate sections stained with hematoxylin & eosin. Verhoeff elastin staining of the aorta was performed to evaluate the number and mean thickness of elastic lamina and thickness of the tunica media averaged from 4 separate radial locations. Elastin fragmentation was scored blinded to treatment as 0 = none, 1 = minimal, 2 = mild, 3 = moderate, or 4 = severe.

Plasma and urine biomarkers. Plasma angiotensin II concentrations were determined using an enzyme immunoassay (SPI-BIO, Montigny le Bretonneux, France) with an Ellman's chromagenic reagent that has a minimum detectable concentration of 1 pg/ml. Urinary albumin concentration was quantified by a competitive enzyme-linked immunosorbent assay (Albuwell-M, Exocell, Philadelphia, Pennsylvania).

Statistical methods. Unless otherwise specified, data are presented as mean ± SD. Effects of treatment were assessed with a paired *t* test for normally distributed variables. Group comparisons were made with 1-way analysis of variance with *t* tests for independent samples and Bonferroni correction. Scored histopathology data were evaluated using either a Kruskal-Wallis test or a Mann-Whitney test for intergroup comparisons. rt-PCR data were compared with a Mann-Whitney test. A p value of <0.05 was considered significant. Since within each treatment group there were no significant differences between wild-type and double-knockout mice for any baseline or post-treatment hemodynamic or echocardiographic parameters, data were combined for the 2 groups.

Results

Cardiovascular and hemodynamic effects of VEGF inhibition. In sham-treated mice, there were no significant changes in LV dimensions, mass, or echocardiographic measures of systolic function over the 5-week treatment period (Table 1). Inhibition of VEGF with G6-31 for 5 weeks produced a significant increase in LV wall thickness and mass, and a decrease in end-diastolic diameter consistent with concentric hypertrophy. The presence of hypertrophy in G6-31 compared with control mice was further supported by larger myocyte cross-sectional area (122 ± 15 μm^2 vs. 100 ± 13 μm^2, p = 0.04) and higher ventricular expression of β-MHC, ANP, and BNP mRNA on rtPCR (Online Fig. A), although myocardial collagen area on histology was similar (2.7 ± 1.1% vs. 2.8 ± 1.3%, p = 0.91; n = 6 each; examples shown in Online Fig. B). In G6-31–treated animals, there was also a reduction in thickening fraction, SV, and velocity of circumferential shortening (VcF) (Table 1). All of the changes in ventricular size and function in G6-31–treated mice were completely attenuated by ramipril co-administration.

Table 1 Echocardiography Data

	Control (n = 18)		G6-31 (n = 18)		G6-31+Ramipril (n = 14)	
	Week 0	Week 5	Week 0	Week 5	Week 0	Week 5
$LVID_d$, mm	3.4 ± 0.2	3.3 ± 0.2	3.4 ± 0.2	3.1 ± 0.3*	3.6 ± 0.3	3.5 ± 0.4
$LVID_s$, mm	2.3 ± 0.2	2.4 ± 0.3	2.3 ± 0.3	2.4 ± 0.3	2.5 ± 0.3	2.6 ± 0.4
WT_d, mm	0.66 ± 0.09	0.68 ± 0.09	0.65 ± 0.09	0.79 ± 0.06†‡	0.66 ± 0.12	0.68 ± 0.08
LV mass, mg	66 ± 13	66 ± 12	66 ± 12	73 ± 8*	67 ± 13	68 ± 13
Thickening fraction	0.56 ± 0.14	0.53 ± 0.15	0.63 ± 0.19	0.38 ± 0.12*	0.54 ± 0.21	0.42 ± 0.11
SV, μl	50 ± 16	40 ± 10	45 ± 10	31 ± 7*	45 ± 12	42 ± 24
VcF, mm/s	0.66 ± 0.15	0.60 ± 0.17	0.69 ± 0.13	0.48 ± 0.18*	0.54 ± 0.12	0.49 ± 0.17
S', mm/s	15.8 ± 4.6	12.9 ± 4.7*	15.2 ± 3.0	12.3 ± 4.7*	15.6 ± 2.7	12.2 ± 4.9*
E', mm/s	12.3 ± 4.2	9.7 ± 5.3*	13.6 ± 5.6	9.7 ± 2.7*	13.6 ± 5.7	10.3 ± 3.3*

Values are mean ± SD. *p < 0.05 versus week 0 data; †p < 0.05 versus week 0 data and versus week 5 control and G6-31+ramipril (corrected for multiple comparisons); ‡p < 0.05 versus control and G6-31+ramipril with respect to change in value from week 0 to week 5.

E' = peak early diastolic endocardial velocity; LVID = left ventricular internal dimension; S' = peak systolic endocardial velocity; SV = stroke volume; VcF = velocity of circumferential fiber shortening; WT_d = diastolic wall thickness.

Table 2 Hemodynamics and Aortic Mechanical Properties

	Control (n = 12)	G6-31 (n = 10)	G6-31+Ramipril (n = 9)
SBP, mm Hg	99 ± 7	108 ± 9*	98 ± 6
DBP, mm Hg	65 ± 8	76 ± 8*	66 ± 8
LV+dp/dt, mm Hg/s	9,070 ± 1,995	10,508 ± 1,407	8,042 ± 1,660
LV−dp/dt, mm Hg/s	−7,320 ± 2,245	−8,624 ± 2,369	−7,469 ± 2,283
Elastic modulus, KPa	28.0 ± 8.3	31.3 ± 8.5	29.3 ± 10.1
E_A, mm Hg/μl	3.4 ± 1.0	4.4 ± 1.3†	3.7 ± 1.7

Values are mean ± SD. *p < 0.05 versus control and G6-31+ramipril; †p < 0.05 versus control only. Abbreviations as in Table 1.

On endocardial tissue Doppler imaging, there was a mild age-dependent decrease in S′ and E′, the degree of which was not significantly different between treatment groups.

On invasive hemodynamic evaluation, G6-31–treated mice had higher SBP, diastolic blood pressure, and peak positive and negative LV dp/dt than either the control or G6-31+ramipril cohort (Table 2). The degree of hypertension caused by G6-31 was even more prominent on conscious ambulatory recordings with a 17 ± 11%, 25 ± 11%, and 38 ± 11% increase in SBP for weeks 1, 2, and 3 of therapy, respectively (analysis of variance $p < 0.01$), after which blood pressures stabilized. Ambulatory blood pressures were constant over time in sham-treated mice. Elastic modulus of the aorta was similar between treatment groups, whereas arterial elastance was significantly greater in G6-31–treated mice (Table 2), indicating a marked increase in afterload without any major alterations in the mechanical properties of the aorta. On aortic histology, medial thickness and indices of elastin content were not different in G6-31–treated compared with control mice (Fig. 1). There was a nonsignificant trend toward more elastin fragmentation in G6-31–treated mice, although the degree of fragmentation was mild or less in all animals. Post-treatment plasma angiotensin II concentration was higher in G6-31–treated compared with control mice (47 ± 17 pg/ml vs. 78 ± 36 pg/ml, p = 0.01, n = 12 each), whereas myocardial

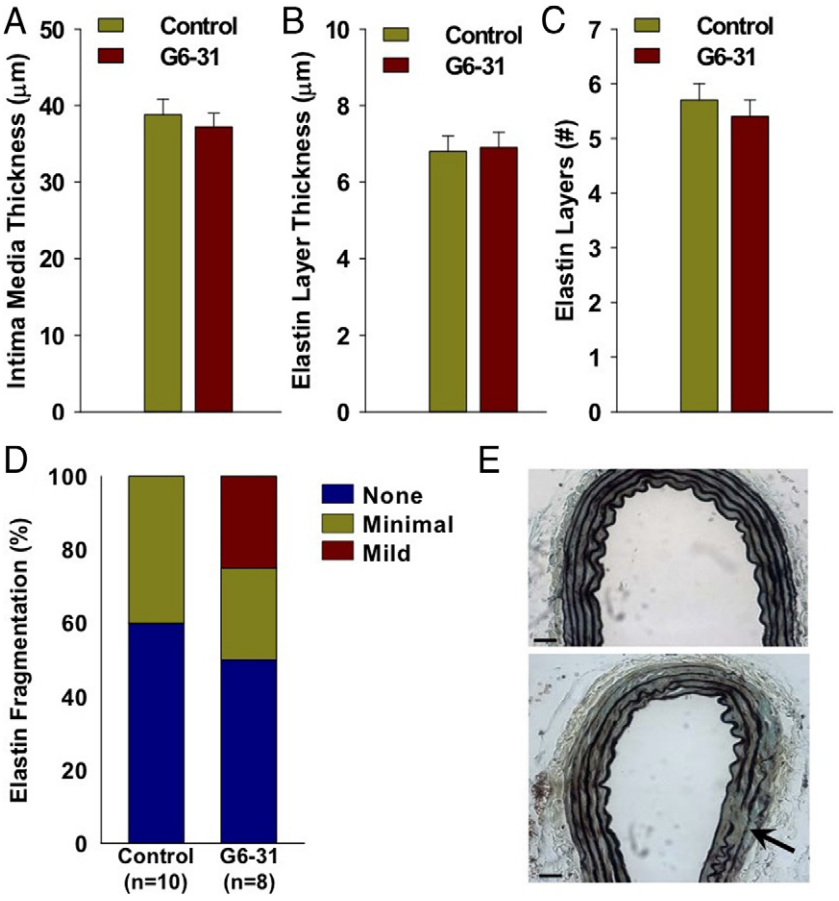

Figure 1 Ascending Thoracic Aorta Histology

Mean (±SEM) **(A)** thickness of the tunica media, **(B)** number of elastic lamina, and **(C)** elastin layer thickness for control and G6-31–treated mice after 5 weeks of therapy. **(D)** Elastic lamina fragmentation scores, expressed as a proportion for each score. p = NS by Mann-Whitney and chi-square analysis. **(E)** Elastin staining of the ascending aorta illustrating normal **(top)** and mild fragmentation **(bottom, arrow)** of the elastic laminae. Scale bar = 20 μm. Four measurements were made for 8 mice in each group.

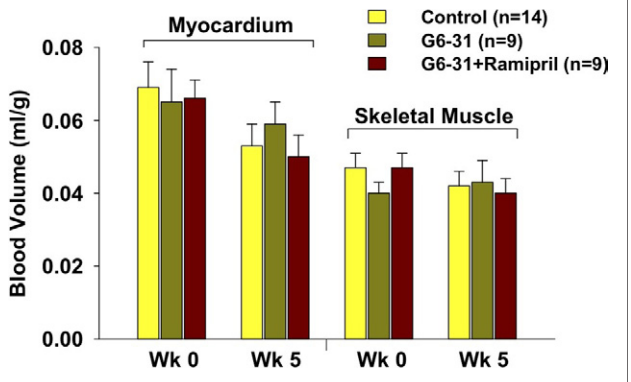

Figure 2 **Mean (±SEM) MBV in the Myocardium and Skeletal Muscle**

Volumes were measured at baseline (Wk 0) and after 5 weeks of therapy (Wk 5). Microvascular blood volume (MBV) for skeletal muscle represents values calculated for the capillary compartment.

rt-PCR for phosphorylated eNOS was not significantly different between groups (0.20 ± 0.01 vs. 0.23 ± 0.03, p = 0.12; n = 5 each).

MBV and MBF. Functional MBV in the LV myocardium at baseline and after therapy were similar between treatment groups (Fig. 2). For all groups, there was a nonsignificant trend for an age-related decrease in myocardial MBV. Functional MBV in skeletal muscle at baseline and after therapy was similar between the treatment groups and did not change with age (Fig. 2). Skeletal muscle MBF at baseline and after 5 weeks of therapy was also similar between the treatment groups (Fig. 3A), as was hyperemic MBF during contractile exercise measured at 5 weeks (Fig. 3B). Skeletal muscle microvascular density on immunohistochemistry was similar for control and G6-31–treated mice (1.3 ± 0.9 vs. 1.2 ± 0.6 $\times 10^{-3}$ fractional area; examples shown in Online Fig. C).

Renal perfusion and histology. Renal vascular resistance measured after completion of treatment was significantly increased in G6-31–treated compared with control animals (37 ± 12 vs. 27 ± 13 mm Hg·min·g/ml, $p < 0.05$), and was significantly reduced in G6-31–treated mice when also treated with ramipril (15 ± 10 mm Hg·min·g/ml). Treatment with G6-31 increased both urinary albumin excretion and serum creatinine (Fig. 4). On histology, cortical glomerular pathology was present in the majority of animals treated with G6-31, which ranged from a focal increase in mesangial matrix to severe diffuse glomerulosclerosis associated with dense fibrin deposition (Figs. 4C and 5, Online Fig. D). These changes were isolated to nephrons in the outer cortex. There was a nonsignificant trend toward less glomerular pathology in the G6-31+ramipril group (Fig. 4C). There was no evidence for tubulointerstitial disease.

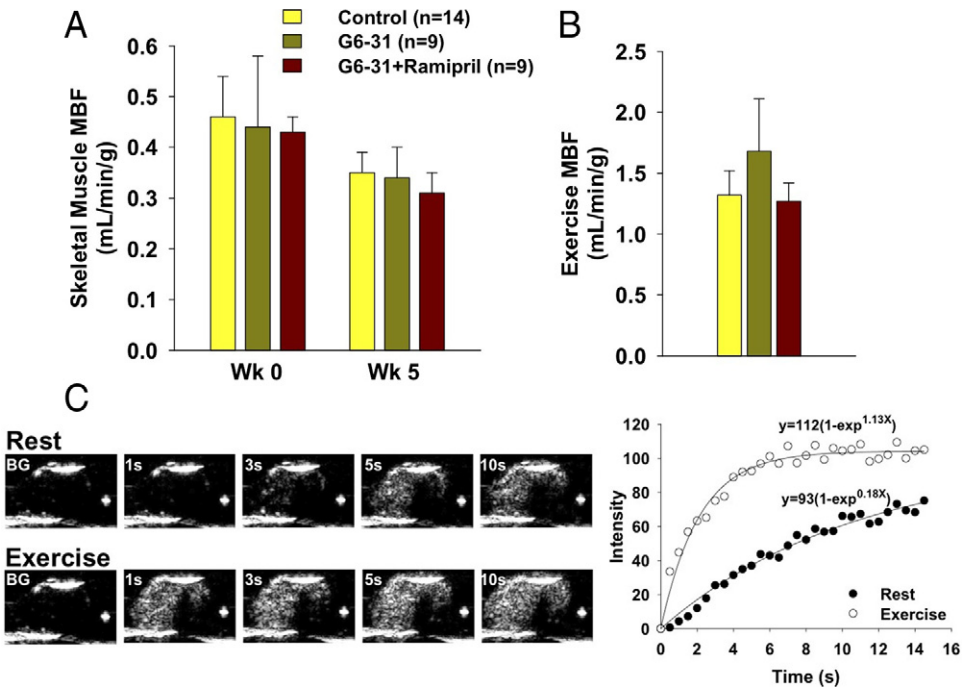

Figure 3 **Skeletal Muscle MBF**

(A) Mean (±SEM) microvascular blood flow (MBF) at rest. **(B)** Mean (±SEM) MBF during contractile exercise measured after 5 weeks of therapy. **(C)** Examples of contrast-enhanced ultrasound images from the proximal hindlimb obtained after the high-power destructive pulse sequence and corresponding time-intensity data at rest and during contractile exercise. BG = background image.

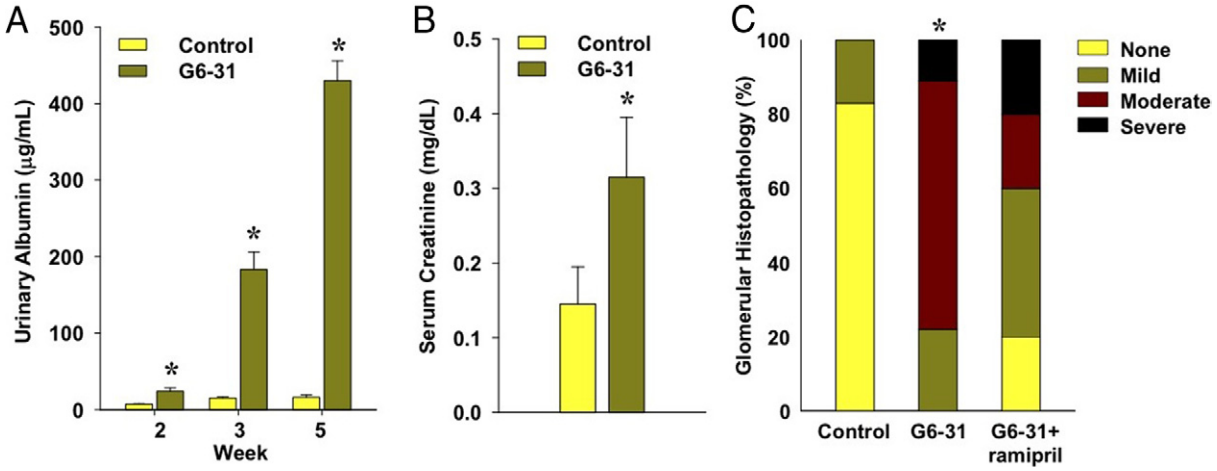

Figure 4 Renal Function and Histology

(A) Mean (±SEM) urinary albumin excretion at weeks 2 to 5 of therapy. **(B)** Serum creatinine at the end of 5 weeks of therapy. $p < 0.05$ versus controls. **(C)** Histopathology scores for glomerular disease; $p < 0.001$ by Kruskal-Wallis test for treatment-related differences. *$p < 0.05$ versus controls for intergroup comparisons; $n = 6$ for all treatment groups.

Discussion

Angiogenesis and remodeling of the existing vascular circuit play a critical role in solid tumor growth, invasion, and metastasis. Antiangiogenic agents have been developed as treatments for cancer therapy. The VEGF-A family of growth factors have been therapeutically targeted by either direct antibody-based inhibition of VEGF or small molecule, broad-spectrum inhibitors of receptor tyrosine kinases that include VEGF receptors. The most frequent side effect of these therapies is clinically significant and sometimes persistent hypertension (2–4). The aim of this study was to employ advanced noninvasive cardiovascular and microvascular imaging methods to characterize potential mechanisms responsible for hypertension and the cardiovascular adaptations that follow.

We studied animals after 5 weeks of therapy with an anti-VEGF-A antibody given at a dose 2-fold higher than maximally effective doses for inhibiting tumor xenograft growth in mice (20). Therapy with G6-31 resulted in systemic hypertension in anesthetized and in conscious ambulatory mice. Aortic histology and elastic modulus suggested that alterations in the mechanical properties of the great vessels did not play a major role. Arterial elastance, reflecting the arterial pressure–SV relation, was substantially higher in G6-31–treated mice, indicating an increased afterload state (17), which was associated with an increase in LV mass, concentric hypertrophy, and a decline in both SV and VcF. Integration of echocardiographic and hemodynamic data indicated that the decline in SV and VcF were probably due to increased afterload rather than a decrease of LV systolic function or contractility. In other words, the increase in afterload with VEGF inhibition led to greater end-systolic wall stress that produces a predictable decrease in VcF according to the force–velocity relation (21). The similar post-treatment values for LV dp/dt and for the end-systolic pressure to LV dimension relation, a surrogate for end-systolic elastance, between groups argues against any reduction in LV contractility or systolic function.

One of the primary aims of our study was to examine whether reduced functional capillary density plays a role in the systemic hypertension during anti-VEGF therapy. The use of CEU in the current study adds important new information on *functional* capillary density in tissues other than the skin. In many major vascular beds, only a fraction of capillaries are actively perfused under resting conditions (15,16,22). CEU can quantify MBV and has been used to evaluate the adequacy of microvascular recruitment in response to physiological states such as exercise and physiological hyperinsulinemia that require an increase in muscle or myocardial capillary surface area for nutrient delivery (15,16). This was the first study to our knowledge to examine reduced *functional* capillary density as a cause of hypertension from VEGF inhibitors. We failed to find any reduction in functional myocardial or skeletal muscle capillary density. The age-related decrease in myocardial MBV likely reflected parallel age-related trends in LV function, and hence oxygen demand.

Our CEU measurements of MBV and myocardial phosphorylated eNOS do not necessarily exclude a role of reduced NO availability in VEGF-inhibitor hypertension. NO-mediated vasodilation, including through VEGF signaling, may still be important in regulation of peripheral arterial tone (11). However, our studies are complementary to prior studies in that they exclude significant functional microvascular rarefaction but also implicate increased plasma angiotensin II in the development of hypertension

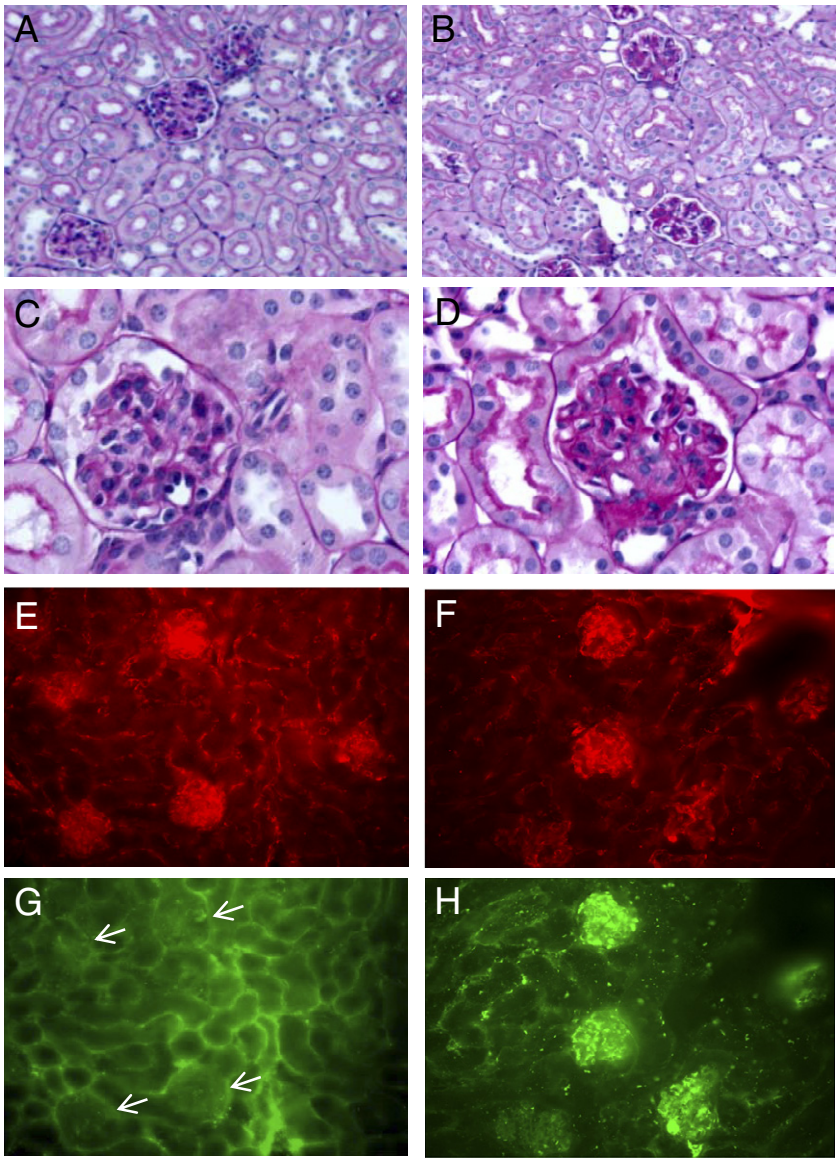

Figure 5 **Examples of Histopathology From the Outer Renal Cortex From Control and G6-31–Treated Mice**

(A, C, E, and G) Control mice and **(B, D, F, and H)** G6-31–treated mice. Examples include periodic acid–Schiff (PAS) staining **(A to D)**, endothelial staining with CD31 **(E and F)**, and fibrin staining (**G** and **H** representing sections that were directly adjacent to corresponding CD31 staining sections). The PAS staining examples show glomeruli that were graded as normal **(A and C)** and severe mesangial change **(B and D)**. **Arrows (G)** illustrate the location of nonstaining glomeruli that are clearly visible by CD31 staining **(E)**. Examples of PAS staining for G6-31 mice and fibrin/CD31 overlay images with confocal microscopy are provided in the Online Appendix.

and ventricular remodeling during VEGF inhibition. The angiotensin-converting enzyme inhibitor ramipril had a salutary effect on almost all cardiovascular and hemodynamic derangements in G6-31–treated mice, although this does not necessarily imply that angiotensin II was the only mediator of hypertension.

With regard to the renal changes, the interaction of angiotensin and NO in regulating afferent and efferent arteriolar tone, renal blood flow, and glomerular filtration rate has been well characterized (23). It is feasible that altered renal afferent–efferent arteriolar resistance balance from high plasma angiotensin II, possibly in combination with low NO production, may have had a role in the development of proteinuria and the increase in renal vascular resistance in G6-31–treated mice. Inhibition of VEGF has also been associated with glomerular endothelial alterations and a thrombotic microangiopathy (13,14). We observed outer cortical glomerular mesangial proliferation after G6-31 and diffuse fibrin deposition, which has been previously described with VEGF inhibition (14,24). There was no evidence for advanced thrombotic microangiopathy that has also been described, possibly because of study-

related differences in mechanism and/or duration of VEGF inhibition. Whether the glomerular structural and functional abnormalities were due to altered afferent/efferent vasoregulatory balance, direct glomerular effects of VEGF, or simply to the hypertension is not clear. However, we did observe that treatment with ramipril had a salutary effect on renal pathologic changes and especially on renal vascular resistance.

Study limitations. First, we did not evaluate the effect of either dose or duration of anti-VEGF therapy. We believe the 5-week time interval is appropriate to study the determinants of hypertension, given the temporal course of hypertension in humans. However, it has been shown that angiogenesis is important in the response to pressure overload (25), so that longer studies may have revealed progression to systolic functional decline associated with a decrease in functional myocardial MBV. The dose of G6-31 was based on previous studies evaluating efficacy of neovascularization in murine tumor models (20). The lack of increased myocardial collagen in the G6-31–treated animals was an unexpected finding if we believe that angiotensin II may have played a role in LV remodeling during VEGF inhibition. It is possible that this finding reflects the short treatment duration.

The most important limitation of this study is that we have not provided evidence for any 1 mechanism for hypertension during anti-VEGF therapy. We believe that the process is likely complex and multifactorial. However, we have shown that antibody-mediated VEGF inhibition produces rapid-onset hypertension, increased afterload, and LV remodeling with reduced SV, but without impairment in LV systolic function or contractility. We have also excluded the pathophysiological contributions from functional capillary loss in large microvascular beds or abnormal arterial elastic properties. We have also detected an increase in plasma angiotensin II and that angiotensin-converting enzyme inhibitors appear to be an effective preventive strategy against, not only the hypertension, but also the adverse cardiac effects of VEGF inhibition.

Reprint requests and correspondence: Dr. Jonathan R. Lindner, Cardiovascular Division, UHN-62, Oregon Health & Science University, 3181 SW Sam Jackson Park Road, Portland, Oregon 97239. E-mail: lindnerj@ohsu.edu.

REFERENCES

1. Duda DG, Batchelor TT, Willett CG, Jain RK. VEGF-targeted cancer therapy strategies: current progress, hurdles and future prospects. Trends Mol Med 2007;13:223–30.
2. Kamba T, McDonald DM. Mechanisms of adverse effects of anti-VEGF therapy for cancer. Br J Cancer 2007;96:1788–95.
3. Hurwitz H, Fehrenbacher L, Novotny W, et al. Bevacizumab plus irinotecan, fluorouracil, and leucovorin for metastatic colorectal cancer. N Engl J Med 2004;350:2335–42.
4. Shord SS, Bressler LR, Tierney LA, Cuellar S, George A. Understanding and managing the possible adverse effects associated with bevacizumab. Am J Health Syst Pharm 2009;66:999–1013.
5. Motzer RJ, Rini BI, Bukowski RM, et al. Sunitinib in patients with metastatic renal cell carcinoma. JAMA 2006;295:2516–24.
6. Kamba T, Tam BY, Hashizume H, et al. VEGF-dependent plasticity of fenestrated capillaries in the normal adult microvasculature. Am J Physiol Heart Circ Physiol 2006;290:H560–76.
7. Inai T, Mancuso M, Hashizume H, et al. Inhibition of vascular endothelial growth factor (VEGF) signaling in cancer causes loss of endothelial fenestrations, regression of tumor vessels, and appearance of basement membrane ghosts. Am J Pathol 2004;165:35–52.
8. Tang K, Breen EC, Gerber HP, Ferrara NM, Wagner PD. Capillary regression in vascular endothelial growth factor-deficient skeletal muscle. Physiol Genomics 2004;18:63–9.
9. Steeghs N, Rabelink TJ, op 't Roodt J, et al. Reversibility of capillary density after discontinuation of bevacizumab treatment. Ann Oncol 2010;21:1100–5.
10. Horowitz JR, Rivard A, van der Zee R, et al. Vascular endothelial growth factor/vascular permeability factor produces nitric oxide-dependent hypotension. Evidence for a maintenance role in quiescent adult endothelium. Arterioscler Thromb Vasc Biol 1997;17:2793–800.
11. Facemire CS, Nixon AB, Griffiths R, Hurwitz H, Coffman TM. Vascular endothelial growth factor receptor 2 controls blood pressure by regulating nitric oxide synthase expression. Hypertension 2009;54:652–8.
12. Kappers MH, van Esch JH, Sluiter W, Sleijfer S, Danser AH, van den Meiracker AH. Hypertension induced by the tyrosine kinase inhibitor sunitinib is associated with increased circulating endothelin-1 levels. Hypertension 2010;56:675–81.
13. Eremina V, Sood M, Haigh J, et al. Glomerular-specific alterations of VEGF-A expression lead to distinct congenital and acquired renal diseases. J Clin Invest 2003;111:707–16.
14. Eremina V, Jefferson JA, Kowalewska J, et al. VEGF inhibition and renal thrombotic microangiopathy. N Engl J Med 2008;358:1129–36.
15. Dawson D, Vincent MA, Barrett EJ, et al. Vascular recruitment in skeletal muscle during exercise and hyperinsulinemia assessed by contrast ultrasound. Am J Physiol Endocrinol Metab 2002;282:E714–20.
16. Le DE, Bin JP, Coggins MP, Wei K, Lindner JR, Kaul S. Relation between myocardial oxygen consumption and myocardial blood volume: a study using myocardial contrast echocardiography. J Am Soc Echocardiogr 2002;15:857–63.
17. Kelly RP, Ting CT, Yang TM, et al. Effective arterial elastance as index of arterial vascular load in humans. Circulation 1992;86:513–21.
18. Behm CZ, Kaufmann BA, Carr C, et al. Molecular imaging of endothelial vascular cell adhesion molecule-1 expression and inflammatory cell recruitment during vasculogenesis and ischemia-mediated arteriogenesis. Circulation 2008;117:2902–11.
19. Wei K, Jayaweera AR, Firoozan S, Linka A, Skyba DM, Kaul S. Quantification of myocardial blood flow with ultrasound-induced destruction of microbubbles administered as a constant venous infusion. Circulation 1998;97:473–83.
20. Liang WC, Wu X, Peale FV, et al. Cross-species vascular endothelial growth factor (VEGF)-blocking antibodies completely inhibit the growth of human tumor xenografts and measure the contribution of stromal VEGF. J Biol Chem 2006;281:951–61.
21. Glick G, Sonnenblick EH, Braunwald E. Myocardial force-velocity relations studied in intact unanesthetized man. J Clin Invest 1965;44:978–88.
22. Honig CR, Odoroff CL, Frierson JL. Capillary recruitment in exercise: rate, extent, uniformity, and relation to blood flow. Am J Physiol 1980;238:H31–42.
23. Patzak A, Persson AE. Angiotensin II-nitric oxide interaction in the kidney. Curr Opin Nephrol Hypertens 2007;16:46–51.
24. Hara A, Wada T, Furuichi K, et al. Blockade of VEGF accelerates proteinuria, via decrease in nephrin expression in rat crescentic glomerulonephritis. Kidney Int 2006;69:1986–95.
25. Shiojima I, Sato K, Izumiya Y, et al. Disruption of coordinated cardiac hypertrophy and angiogenesis contributes to the transition to heart failure. J Clin Invest 2005;115:2108–18.

Key Words: contrast echocardiography ■ VEGF ■ ventricular hypertrophy.

APPENDIX

For an expanded Methods section and supplementary figures, please see the online version of this paper.